Successive Magnetic Phase Transitions of Component Orderings in DyB_4

Takeshi MATSUMURA[1,2], Daisuke OKUYAMA[3], Takuya MOURI[4], and Youichi MURAKAMI[5]

[1]*Department of Quantum Matter, AdSM, Hiroshima University, Higashi-Hiroshima, Hiroshima 739-8530*
[2]*Institute for Advanced Materials Research, Hiroshima University, Higashi-Hiroshima, Hiroshima 739-8530*
[3]*Cross-Correlated Materials Research Group (CMRG), ASI, RIKEN, Wako, Saitama 351-0198*
[4]*Department of Physics, Graduate School of Science, Tohoku University, Sendai 980-8578*
[5]*Institute of Materials Structure Science, High Energy Accelerator Research Organization, Tsukuba, Ibaraki 305-0801*

The successive magnetic phase transitions in DyB_4 have been studied in detail by microscopic measurements using resonant X-ray diffraction and neutron scattering. It is shown that the *ab*-plane component of the magnetic moment is short-range-ordered in the intermediate phase where the *c*-axis component is long-range-ordered. It is estimated that this short-range order is dynamically fluctuating with a time scale between $\sim 10^{-8}$ to $\sim 10^{-11}$ s. Crystal field excitation has also been investigated by inelastic neutron scattering. To qualitatively understand the phase-transition phenomenon, we have studied a simple two-sublattice model with an antiferromagnetic interaction by mean-field calculation. The calculation, though without a quadrupolar interaction, successfully explains the occurrence of double phase transition, magnetic specific heat and entropy, magnetic susceptibility, and the huge elastic softening in the intermediate phase. The general success of the mean-field calculation, except for the short-range order, suggests that there is little effect of geometrical frustration on the macroscopic properties at zero magnetic field.

Journal Ref: J. Phys. Soc. Jpn., **80**, 074701 (2011).
http://dx.doi.org/10.1143/JPSJ.80.074701

KEYWORDS: DyB_4, successive magnetic transitions, component ordering, geometrical frustration

1. Introduction

Geometrically frustrated magnetic materials have attracted much interest because of their exotic ordering phenomena. A macroscopic number of degenerate ground states disturb long-range order (LRO) down to very low temperatures. Even when the system exhibits a LRO by second- and further-neighbor interactions, the ordering process sometimes becomes quite exotic. A successive phase transition is one of such phenomena. Typical examples are ATX_3 (A=alkali metal, T=transition metal, X=halogen) compounds where the T atoms form a triangular lattice. In the intermediate phase of $CsCoCl_3$, between $T_{N1} = 21$ K and $T_{N2} = 9$ K, spins on two of the three sublattices are antiferromagnetically ordered but the rest remains paramagnetic, which is called a partial disordered phase.[1,2] In $CsNiCl_3$, the *c*-axis and *ab*-plane components of the magnetic moments order separately at $T_{N1} = 4.8$ K and $T_{N2} = 4.4$ K, respectively.[3] These behaviors are closely associated with the triangular lattice.

Rare-earth tetraborides, RB_4, have been studied recently as a system in which the geometrical frustration of magnetic dipole and electric quadrupole moments may play important roles. The R ions in RB_4, with a tetragonal structure belonging to the space group $P4/mbm$, form a network in the *ab*-plane that is topologically equivalent to the so called Shastry-Sutherland lattice (SSL),[4] where a spin-singlet ground state can take place in two-dimensional quantum spin systems such as $SrCu_2(BO_3)_2$ with $S = 1/2$.[5] Although RB_4 is a three-dimensional classical moment system with a strong coupling also along the *c*-axis and has relatively large *J*-values, RB_4 compounds attract interest because most of them exhibit successive magnetic transitions.[6] For R=Tb and Tm, the anomalous transitions in magnetic fields have recently been discussed from the viewpoint of frustration.[7–11] The double magnetic transition at zero field for R=Nd, Tb, Dy, and Ho, in addition, are also considered to be associated with the interplay between magnetic dipole and electric quadrupole interactions.[12–16]

The purpose of the present study is to clarify the origin of the double transition in DyB_4 and examine the possibility of a frustration effect that was discussed in previous studies.[14,15,17] DyB_4 is an antiferromagnet with two transitions at $T_{N1} = 20.3$ K and $T_{N2} = 12.7$ K.[14] Below T_{N1}, the *c*-axis component of the magnetic moment orders into a simple collinear antiferromagnetic structure.[15,17,18] The *ab*-plane components order at T_{N2} into a non-collinear structure. Hereafter, the paramagnetic phase above T_{N1} is referred to as phase I, the intermediate phase between T_{N1} and T_{N2} as phase II, and the low-temperature phase below T_{N2} as phase III. What is intriguing is that the softening of the C_{44} mode of the elastic constant is significantly enhanced on entering phase II.[14] Moreover, a strong ultrasonic attenuation occurs in phase II, suggesting a large fluctuation in the quadrupolar moments. This remarkable fluctuation in phase II has also been observed by resonant X-ray diffraction (RXD) as a short-range order (SRO) of $\langle J_x \rangle$, the *ab*-plane component of the magnetic moment, or of the $\langle O_{zx} \rangle$-type electric quadrupole moment.[15] Since the magnetic entropies of $R \ln 2$ and $R \ln 4$ are released at T_{N2} and T_{N1}, respectively, it has been considered that the quadrupolar degeneracy of the pseudo-quartet ground state is not lifted even in the magnetically ordered phase II. The

mechanism of these unusual phenomena and their relation to the SSL in DyB_4 have not been understood yet.

In the present study, we have investigated the successive transitions of DyB_4 by RXD and neutron scattering. After describing the experimental procedure in §2, the experimental results are presented in §3. First, in RXD, the resonant signal is identified as of magnetic dipole origin, which remained unclear in the previous work discussed in ref. 15. Second, by neutron diffraction (ND), the temperature dependence of each magnetic component along the c-axis and ab-plane is deduced, which is consistent with the result of RXD. Third, the dynamical aspect of magnetic moments are investigated by inelastic neutron scattering. Crystal field excitations, low-energy excitations, and critical scattering are described in detail. In §4, the mechanism of double transition is discussed on the basis of a mean-field calculation for a two-sublattice system. We adopt the crystalline electric field (CEF) scheme proposed by Tanaka in which the fourth-order term plays a fundamental role.[19] Magnetic entropy, magnetic susceptibility, and elastic constants can be understood qualitatively by this calculation without consideration of SSL. We discuss the role of SSL in §5, and present the conclusion drawn in the present study in §6.

2. Experimental Procedure

The RXD experiment was performed using a four-circle diffractometer at Beamline 16A2 of the Photon Factory in the High Energy Accelerator Research Organization (KEK), Tsukuba. A sample with a mirror-polished (100) surface was mounted in a helium-gas closed-cycle refrigerator. The incident X-ray was tuned near the $L_{\rm III}$ absorption edge of Dy (∼7.79 keV), where the resonance between the $2p$ and $5d$ orbitals occurs. Polarization analysis was performed using a pyrolytic graphite (PG) analyzer crystal.

A neutron scattering experiment was performed using the Tohoku University triple-axis thermal neutron spectrometer TOPAN installed at the beam hole 6G of the research reactor JRR-3, Japan Atomic Energy Agency, Tokai. A monochromatized incident beam was obtained using the 002 Bragg reflection of PG crystals. The energy of the scattered beam was also analyzed using a PG-002 analyzer. Neutrons with higher harmonic energies were cut with PG filters. The conditions of the collimators and neutron energies are shown in the corresponding figures.

Single-crystalline samples were grown by the floating zone method using a high-frequency furnace. For neutron scattering experiments, an enriched ^{11}B isotope was used to prevent the absorption of neutrons by the ^{10}B isotope contained in natural boron. Then, the severe absorption coefficient of 767 barn for natural boron was reduced to a negligible level. However, the absorption by natural dysprosium (994 barn) was not prevented because of the cost and the availability of Dy isotope; 994 barn means that 86% of the incident neutrons are absorbed by a sample with a thickness of 1 mm. To overcome this severe difficulty, we sliced the sample into plates with a thickness of 0.5 mm to make the scattering probability maximum. We prepared four such plates and aligned them together in the same orientation so that the diffraction peaks form a single peak. The widths of the rocking scan for each sample ranged from 0.3 to 0.5°, and the final width of the aligned samples was 0.54°.

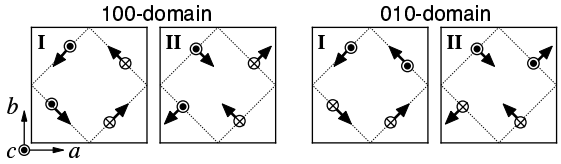

Fig. 1. Two models (I and II) of the magnetic structure of DyB_4 and their domain states.

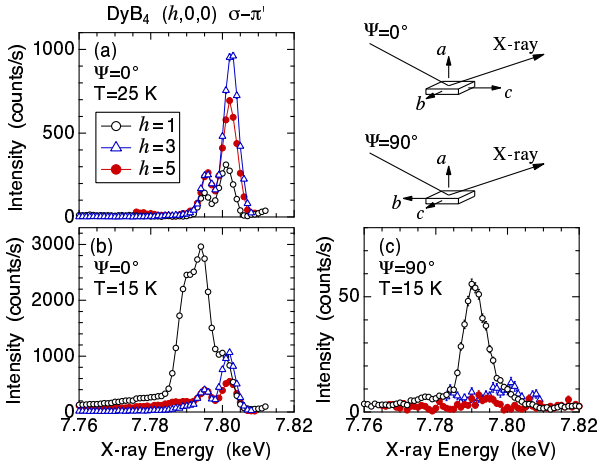

Fig. 2. (Color online) Incident energy dependences of the peak-top intensity of the (h, 0, 0) reflection for σ-π' at (a) $\Psi = 0°$ and $T = 25$ K in phase I, (b) $\Psi = 0°$ and $T = 15$ K in phase II, and (c) $\Psi = 90°$ and $T = 15$ K in phase II. Scattering geometries for $\Psi = 0°$ and $\Psi = 90°$ are shown on the right top corner.

3. Results

3.1 Resonant X-ray diffraction

Two models of magnetic and quadrupolar structures were proposed in ref. 15. The magnetic structures and their domain states are shown in Fig. 1.[20] There are 100- and 010-domains corresponding to the directions of the propagation of the c-axis magnetic component. The quadrupolar structure has a one-to-one correspondence with the magnetic structure through the spin-orbit interaction (see Fig. 17 of ref. 16). The unit cell structure factor of the (h = odd, 0, 0) Bragg reflection for the $E1$ resonance, σ-π' channel, and the 100-domain is written as

$$F_{\sigma\pi'}^{(E1)} = 2k_1 b\cos\theta(\sqrt{2}\langle J_z\rangle\cos\Psi - \langle J_x\rangle\sin\Psi) \mp 2k_2 a\cos\theta(\sqrt{2}\langle O_{22}\rangle\cos\Psi + \langle O_{zx}\rangle\sin\Psi), \quad (1)$$

where $a = \cos(2\pi hx)$ and $b = \sin(2\pi hx)$; $x = 0.3175$ is the position parameter of the $4g$ site of Dy.[21] k_1 and k_2 are constant real numbers and θ is the Bragg angle. The definition of the local xyz-axis is the same as that in ref. 15; the direction of the magnetic moment in the ab-plane is taken as the local x-axis and that along the c-axis as the z-axis. The upper and lower signs correspond

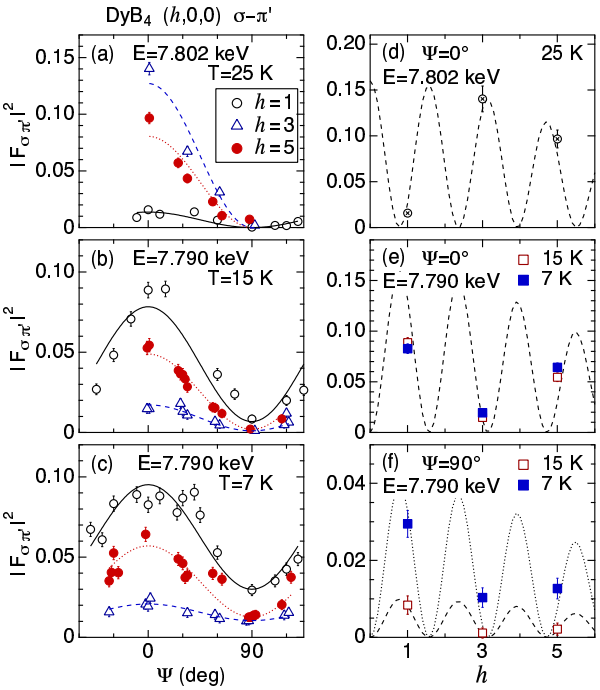

Fig. 3. (Color online) (a), (b), (c) Azimuthal-angle dependences of $|F_{\sigma\pi'}|^2$ at resonance for σ-π' at three temperatures in phases I, II, and III, respectively. The lines are fits to $\cos^2\Psi$ and $\sin^2\Psi$. (d), (e), (f) h dependence of $|F_{\sigma\pi'}|^2$. The line in (d) represents $\cos^2(2\pi hx)\cos^2\theta$ and those in (e) and (f) represent $\sin^2(2\pi hx)\cos^2\theta$.

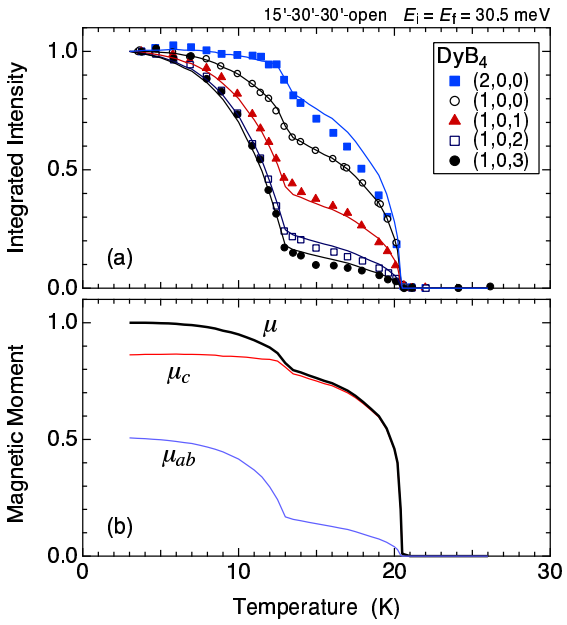

Fig. 4. (Color online) (a) Temperature dependences of the integrated intensities of the magnetic diffraction peaks. The intensities are normalized to unity at the lowest temperature. The lines are calculation results. (b) Temperature dependences of the total magnetic moment μ, and its c-axis and ab-plane components, from which the lines in (a) are calculated.

to models I and II, respectively. The structure factor for the 010-domain is written as

$$F_{\sigma\pi'}^{(E1)} = -2k_1 b\cos\theta\langle J_x\rangle\sin\Psi + 2k_2 a(\mp\sqrt{2}\cos\theta\langle O_{22}\rangle\cos\Psi - \sin\theta\langle O_{zx}\rangle\cos 2\Psi). \quad (2)$$

There is no domain structures for $\langle O_{22}\rangle$ or $\langle J_x\rangle$.

Figure 2 shows the incident energy dependences of the (h, 0, 0) forbidden reflections for the σ-π' channel at 25 K in phase I and at 15 K in phase II. This is an extension of the measurement performed in ref. 15. The result for (1, 0, 0) and its temperature dependence has already been reported in ref. 15. By comparison with the calculated structure factor, it was concluded that the signal at $\Psi = 0°$ reflects $\langle J_z\rangle$ and the signal at $\Psi = 90°$ reflects $\langle J_x\rangle$ or $\langle O_{zx}\rangle$. The point here is that the signal at $\Psi = 90°$ reflecting $\langle J_x\rangle$ or $\langle O_{zx}\rangle$, which orders at T_{N2}, is observed in phase II as a result of SRO.

One remaining problem in RXD is that the origin of the signal, i.e., whether magnetic or quadrupolar origin, has not been identified yet. As shown in eqs. (1) and (2), the signals of the magnetic and quadrupolar origins overlap at the same Ψ. This can be identified by measuring the intensities for higher index h. As shown in Figs. 2(b) and 2(c), the resonance intensity for (3, 0, 0) and (5, 0, 0) is much weaker than that for (1, 0, 0). This is because of the factors a and b in eqs. (1) and (2).

Figure 3 shows the Ψ and h dependences of the structure factor squared for the σ-π' channel, $|F_{\sigma\pi'}|^2$, which was deduced from the integrated intensity of the rocking scan of the resonant peak. The intensity I is proportional to $|F_{\sigma\pi'}|^2$ and can be expressed as $I = \alpha|F_{\sigma\pi'}|^2/\sin\theta$, where $\sin\theta$ is the Lorentz factor. The constant α for (1, 0, 0) was deduced from the (2, 0, 0) fundamental peak, α for (3, 0, 0) from the average of (2, 0, 0) and (4, 0, 0), and α for (5, 0, 0) from the average of (4, 0, 0) and (6, 0, 0), respectively. $|F_{\sigma\pi'}|^2$ in Fig. 3 roughly reflects the absolute value, e.g., $|F|^2$ for the nonresonant Thomson scattering by a Dy atom is $|66|^2$ for the forward scattering.

Figures 3(a) and 3(d) are for the resonant peak at 7.802 keV at 25 K in phase I. This resonance is caused by the anisotropic tensor susceptibility (ATS) scattering that reflects the local anisotropy of the surrounding boron atoms. This gives rise to the $\langle O_{22}\rangle$ term in eqs. (1) and (2), as directly inferred from the crystal structure. Therefore, $|F_{\sigma\pi'}|^2$ due to the ATS scattering exhibits a $\cos^2\Psi$ dependence for Ψ and a $\cos^2(2\pi hx)\cos^2\theta$ dependence for h, which are demonstrated in Figs. 3(a) and 3(d), respectively.

In the same manner, the signals at $\Psi = 0°$ and $\Psi = 90°$ can be identified as of magnetic dipole origin, as demonstrated in Figs. 3(e) and 3(f). The h dependence follows $\sin^2(2\pi hx)\cos^2\theta$, as expected from eqs. (1) and (2). The signal at $\Psi = 0°$ in Fig. 3(e) arises from $\langle J_z\rangle$ of the 100-domain and that at $\Psi = 90°$ in Fig. 3(f) from $\langle J_x\rangle$ of both domains. Thus, the temperature dependences of the intensity and width reported in ref. 15 show that $\langle J_z\rangle$ exhibits a LRO below T_{N1} and $\langle J_x\rangle$ exhibits a SRO below T_{N1}, which develops into a LRO below T_{N2}.

Table I. Squares of the magnetic structure factors for the c-axis and the ab-plane components. There are 100- and 010-domains for the c-axis component.

$\boldsymbol{Q} = (h, 0, l)$	$\lvert F_c^{100}\rvert^2$	$\lvert F_c^{010}\rvert^2$	$\lvert F_{ab}\rvert^2$
(1, 0, 0)	5.645	0	2.823
(2, 0, 0)	0	3.351	0
(1, 0, 1)	1.192	0	2.460
(1, 0, 2)	0.248	0	1.677
(1, 0, 3)	0.066	0	0.954

3.2 Neutron diffraction

From the macroscopic properties of magnetic susceptibility and elastic constant, the ab-plane component seems paramagnetic in phase II.[14] However, in RXD, it is observed as a SRO. This is considered to be due to the difference in the time scale between the measurements. RXD can be considered an instantaneous measurement with a time scale of approximately $10^{-15} \sim 10^{-16}$ s, an inverse of the lifetime of the intermediate state, probing a snapshot of the target. If the time scale of the fluctuation of the SRO is longer than this but much shorter than the inverse of ultrasonic frequency, it seems paramagnetic in the elastic constant measurement. Therefore, using ND, with a time scale of approximately $10^{-12} \sim 10^{-13}$ s for thermal neutrons, it may be possible to estimate the time scale of the fluctuation in more detail.

In order to deduce the c-axis and ab-plane components by ND, we compared the intensities of (1, 0, 0), (2, 0, 0), (1, 0, 1), (1, 0, 2), and (1, 0, 3) reflections. In ND, the scattering probability is proportional to the magnetic component perpendicular to the scattering vector. Therefore, in the (1, 0, l) reflections, the contribution of the ab-plane component to the intensity becomes stronger as the index l increases. This situation is shown in Table I. The structure factors for the ab-plane component become the same for models I and II in Fig. 1.[20] There is no domain for the ab-plane component. For (2, 0, 0), the magnetic structure factor consists of the c-axis component only.

In Fig. 4(a), the temperature dependences of the intensities are shown for the magnetic reflections shown in Table I. The magnetic structure factors for these reflections can be calculated with two parameters, i.e., μ_c and μ_{ab}, which are the c-axis and ab-plane components of the magnetic moment, respectively. If we assume the temperature dependences of μ_c and μ_{ab} as those shown in Fig. 4(b), the intensities of all the magnetic reflections are calculated as those shown by the lines in Fig. 4(a). All of them show good agreements with the experimental data, which strongly supports the notion that the ab-plane component indeed exists in phase II as concluded from the results of RXD. The temperature dependence of μ_{ab} is also consistent with that obtained from RXD.[15]

If the ab-plane component were completely paramagnetic in phase II, there should occur critical scattering at $T_{\rm N2}$ when the moments in the ab-plane are ordered. Figure 5 shows the energy spectrum around the elastic condition at $\boldsymbol{Q} = (1.05, 0, 0)$, slightly away from the Bragg point at (1, 0, 0). It is clearly demonstrated that

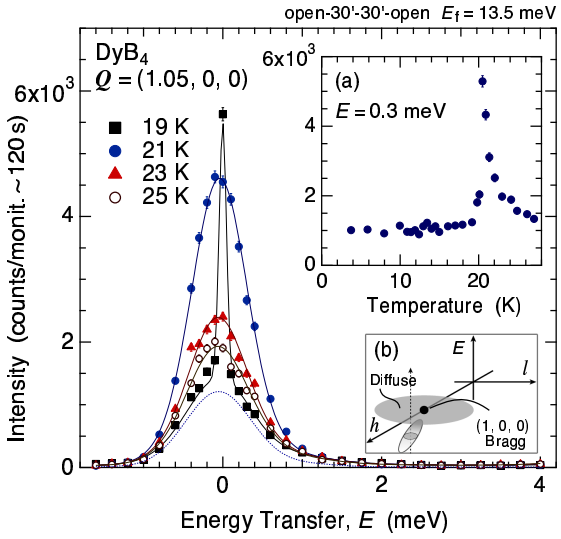

Fig. 5. (Color online) Energy spectrum around the elastic condition for $\boldsymbol{Q} = (1.05, 0, 0)$ at temperatures around $T_{\rm N1}$. The dotted line represents the incoherent scattering that is independent of temperature and the scattering vector. Inset (a) shows the temperature dependence of the intensity measured at the energy transfer of 0.3 meV. Inset (b) is a schematic representation of the energy scan at $\boldsymbol{Q} = (1.05, 0, 0)$, where the resolution ellipsoid passes through the region of diffuse scattering at around $E = 0$.

the incoherent-like scattering around $E = 0$ is enhanced on approaching $T_{\rm N1}$. This is the magnetic critical scattering due to the antiferromagnetic fluctuation of phase II, giving rise to a very broad diffuse scattering around the Bragg point $\boldsymbol{Q} = (1, 0, 0)$. Although this intrinsically has a finite energy width around $E = 0$, it is much smaller than the resolution, and the observed width becomes almost the same as that of the incoherent scattering. At $T = 19$ K below $T_{\rm N1}$ the critical scattering disappears and a Bragg peak appears at $E = 0$; in actuality, this is the tail of the Bragg peak at (1, 0, 0) as seen from the finite resolution width.

The inset (a) of Fig. 5 shows the temperature dependence of the critical scattering as measured at $E = 0.3$ meV. This exhibits a large anomaly at $T_{\rm N1}$. In contrast, no anomaly was observed at $T_{\rm N2}$, which was also the case for other reflection points listed in Table I.[22] These results indicate that the diffuse, or quasi-elastic, scattering due to the fluctuation of the ab-plane component in phase II has shrunk within the energy and $\boldsymbol{Q}$ resolutions of the Bragg peak. From the energy resolution of 0.11 meV for the Bragg peak, we can estimate that the time scale of the fluctuation in phase II is longer than approximately $\hbar/\Delta E \sim 6 \times 10^{-12}$ s.

3.3 Inelastic neutron scattering

We have performed an inelastic neutron scattering experiment to obtain information on CEF excitations and their variation with the phase transitions. The measurement was performed for energy transfer up to 10 meV under the condition of a constant final energy of 13.5 meV. The result is shown in Fig. 6. The magnetic part

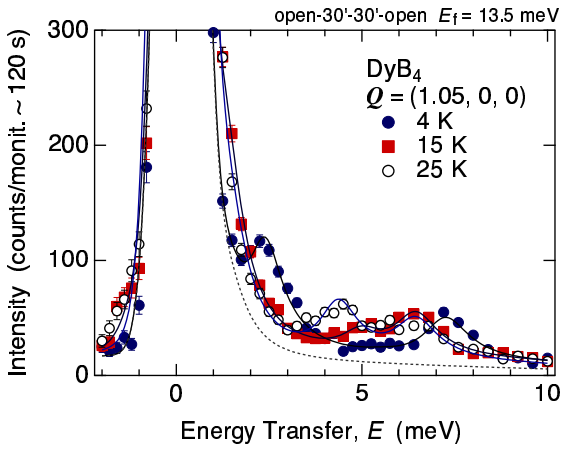

Fig. 6. (Color online) Inelastic neutron scattering spectra for $\boldsymbol{Q}$ = (1.05, 0, 0) at three temperatures in phases I (25 K), II (15 K), and III (4 K). The lines are fits to Lorentzian spectral functions. The dashed line represents the background due to the incoherent scattering.

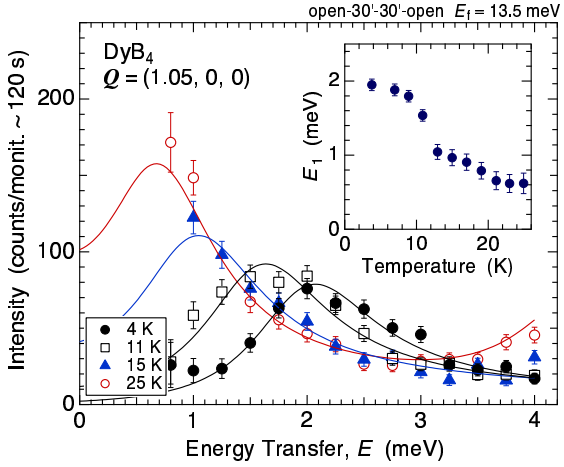

Fig. 7. (Color online) Variation of the low-energy excitation with temperature. Only the magnetic part after the subtraction of the background is shown. The lines are fits to a Lorentzian spectral function. Inset shows the temperature dependence of the excitation energy.

of the excitation has been fitted to the function,

$$S(\boldsymbol{Q}, E) = \frac{E \sum_i f_i P(E; E_i)}{1 - \exp(-E/k_{\mathrm{B}}T)}, \tag{3}$$

where $P(E; E_i)$ represents a Lorentzian spectral function centered at $E = E_i$ and f_i is the strength of the i-th excitation. The width of the Lorentzian was fixed to the instrumental resolution at the corresponding energy because it was difficult to determine the intrinsic width due to the low statistics.

At 25 K in phase I, there are three excitations at E_3 = 6.4 meV, E_2 = 4.3 meV, and below 2 meV. The peak position of the low-energy excitation below 2 meV was estimated to be E_1 = 1.3 meV from the fitting, though it does not show a peak shape because of the overlap with the huge incoherent scattering. At 15 K in phase II, the second peak shifts to 4.9 meV and the intensity decreases. It is noted that the low-energy excitation does not change between phases I and II. On entering phase III, a clear gap appears in the low-energy excitation; a peak structure is clearly observed at approximately 2 meV. The second peak becomes invisible and the third peak shifts to 7.2 meV.

The appearance of the gap in the low-energy excitation on entering phase III can basically be understood as a change in the CEF-level scheme by the magnetic ordering, which will be discussed in the next section. In Fig. 7, we show the variation of the low-energy excitation with temperature after subtracting the incoherent background. The temperature dependence of the excitation energy E_1 is shown in the inset. At high temperatures, since the peak becomes inseparable from the incoherent scattering because of the energy resolution, E_1 was estimated by fixing the width to the instrumental resolution and fitting the tail structure of the spectrum. Of course, more detailed measurement using cold neutrons with higher energy resolution is necessary on this point. Nevertheless, it is possible to state that E_1 exhibits a steep increase on entering phase III below T_{N2}, whereas

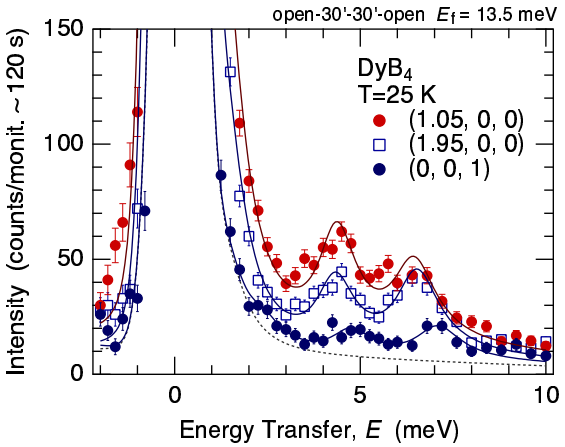

Fig. 8. (Color online) Inelastic neutron scattering spectra at 25 K in phase I for three $\boldsymbol{Q}$-vectors. The lines are fits to Lorentzian spectral functions. The dashed line represents the background due to the incoherent scattering for $\boldsymbol{Q}$ = (0, 0, 1).

it shows only a small increase at T_{N1}. This behavior of E_1 is similar to that of the *ab*-plane magnetic component shown in Fig. 4.

The intensity of the CEF excitation becomes stronger near the magnetic ordering propagation vectors, as shown in Fig. 8. The results for $\boldsymbol{Q}$ = (1.05, 0, 0) and (1.95, 0, 0) are almost identical except for the difference in intensity due to the magnetic form factor. On the other hand, the intensities for $\boldsymbol{Q}$ = (0, 0, 1) are much weaker and the peak positions are slightly shifted to higher energies. This is considered as a result of the magnetic exchange interaction, which will also be discussed in the next section.

4. Mean-Field Model Calculation

4.1 Crystalline electric field

To discuss the origin of the successive transition and analyze the macroscopic properties, let us study if the

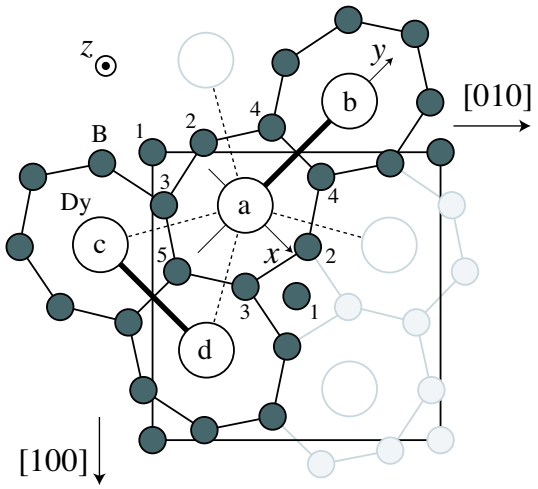

Fig. 9. Top view of the crystal structure of DyB_4. The nearest- and next-nearest-neighbor Dy atoms are linked by the thick solid and dashed lines, respectively. The neighboring B atoms around Dy are filled with dark gray. The numbers represent the order of distance from $Dy^{(a)}$ atom. Dy atoms are on the plane of $z = 0$, $B^{(1)}$ atoms on $z = \pm 0.2c$, and $B^{(2,3,4,5)}$ atoms on $z = \pm 0.5c$, where c is the c-axis lattice constant.

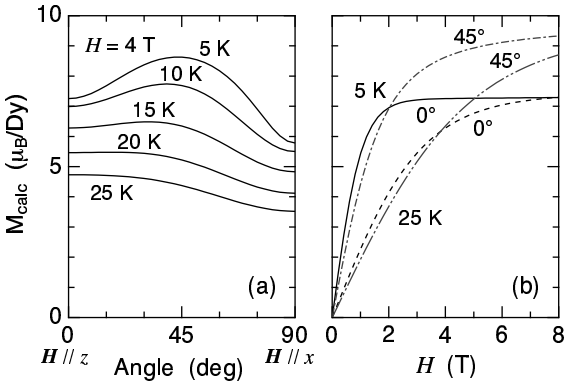

Fig. 10. Calculated magnetization of $Dy^{(a)}$ for the CEF state described in the text. (a) Angle dependences at several temperatures when the applied field of 4 T is rotated from the z-axis (0°) to the x-axis (90°). (b) Magnetic-field dependences at 5 K and 25 K for the field angles of 0° and 45°.

phenomenon can be explained within a mean-field model calculation. First, to calculate the physical properties, we have to define the CEF states of the Dy ion. The Dy^{3+} ion has nine $4f$ electrons and the Hund's rule ground multiplet is expressed by $J = 15/2$, which splits into eight doublets in the CEF. The CEF Hamiltonian for the Dy ion in Fig. 9 can be expressed as an orthorhombic type:

$$\mathcal{H}_{\rm CEF} = \sum_{l=2}^{6} \sum_{m=0}^{l} A_{lm} \theta_J \langle r^l \rangle O_{lm}, \qquad (4)$$

where l and m are even integers, θ_J the Stevens factor, and O_{lm} is the operator equivalent.[23] The local xyz-axis for the Dy ion is shown in Fig. 9, which is the same for $Dy^{(a)}$ and $Dy^{(b)}$, whereas it is rotated by 90° for $Dy^{(c)}$ and $Dy^{(d)}$. Mixing with the $5d$-orbitals due to the lack of inversion symmetry is neglected here.

It is expected that the CEF will be dominated by second-order terms with $l = 2$ in a simplistic consideration such as a point-charge calculation. In this case, one of the x-, y-, and z-axes becomes the easy axis of magnetization; this is the z-axis in DyB_4. Two models may be considered to reproduce the tilting of the ordered moment from the z-axis to the x-axis below $T_{\rm N2}$. One is to introduce a stronger magnetic exchange interaction between the xy components than between the z components to overcome the anisotropy energy. The other is to introduce a ferroquadrupolar exchange interaction between the O_{zx} moments and equivalently between the O_{yz} moments. When the y-axis is the hardest axis of magnetization, the ordered moment along the z-axis will tilt to the x-axis below a certain temperature to gain the quadrupolar exchange energy at the cost of the anisotropy energy. However, these models cannot explain the magnetic susceptibility for $H \perp c$ below $T_{\rm N1}$, which keep increasing with decreasing temperature; the calculation inevitably exhibits a cusp.

The third model for explaining the successive transition is to introduce fourth-order terms as large as the second-order terms, the importance of which has been pointed out by Tanaka.[19] The role of the fourth-order term is to modify the easy axis of magnetization from the z-axis to somewhere in between the z- and x-axes. Let us assume the CEF parameters for $Dy^{(a)}$ as $A_{20}\langle r^2 \rangle = 100$ K, $A_{22}\langle r^2 \rangle = 120$ K, $A_{40}\langle r^4 \rangle = -110$ K, and $A_{42}\langle r^4 \rangle = A_{44}\langle r^4 \rangle = 0$ K. The resultant CEF energy levels are 0 – 16.8 – 42.0 – 83.7 – 141 – 148 – 187 – 240 K. The characteristics of the magnetic anisotropy for this CEF are demonstrated in Fig. 10. We see that $M_{\rm calc}$ for the 45° direction becomes the largest in the low-temperature and high-field region. On the other hand, in the high-temperature and low-field region, $M_{\rm calc}$ for the 0° direction ($\boldsymbol{H} \parallel z$) becomes the largest. Therefore, the first transition at $T_{\rm N1}$ occurs with the z-axis component to achieve the maximum exchange energy. With decreasing temperature, the ordered moment and exchange field increase. When the exchange field increases to about 4 T and the temperature decreases below 15 K, the x-component takes part in the ordering to achieve a larger ordered moment and a larger gain in the exchange energy. This is the second ordering at $T_{\rm N2}$.

4.2 CEF excitation by inelastic neutron scattering

The three magnetic excitations in Fig. 6 at 25 K are qualitatively consistent with this CEF-level scheme. By comparison with the calculated transition strength, it is possible to associate the low-energy excitation below 2 meV with the excitation from the ground state to the first excited level at 16.8 K, the excitation at 4.3 meV from the ground state to the second excited level at 42.0 K, and the excitation at 6.4 meV from the first excited level to the third excited level at 83.7 K. This situation is illustrated in the energy-level diagram in Fig. 12(c), which will be explained in the next subsection. The calculated transition strength for the excitation from the ground state to the third excited level is negligible. The pseudo-quartet discussed in ref. 14 is considered a com-

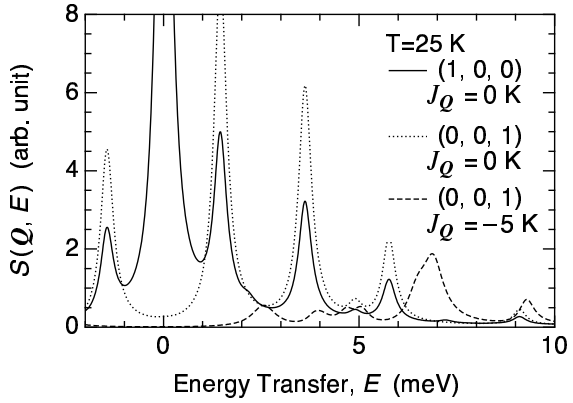

Fig. 11. Calculated inelastic neutron scattering function $S(\boldsymbol{Q}, E)$ at 25 K. The width of the Lorentzian spectral functions are fixed at 0.2 meV.

plex composed of the ground state and first excited level here.

The weak intensity and shift of the peak position for $\boldsymbol{Q} = (0, 0, 1)$ shown in Fig. 8 can be explained by the magnetic exchange interaction. The neutron magnetic scattering function can generally be expressed as

$$S(\boldsymbol{Q}, E) = \sum_{\alpha,\beta} \frac{(\delta_{\alpha\beta} - \tilde{Q}_\alpha \tilde{Q}_\beta)\chi''_{\alpha\beta}(\boldsymbol{Q}, E)}{1 - \exp(-E/k_{\rm B}T)}, \tag{5}$$

where α and β represent x, y, and z. $\tilde{\boldsymbol{Q}}$ is the unit vector of $\boldsymbol{Q}$. $\chi''(\boldsymbol{Q}, E)$ is the imaginary part of the generalized magnetic susceptibility. In mean-field (random phase) approximation, $\chi(\boldsymbol{Q}, E)$ can be expressed as

$$\chi_{\alpha\beta}(\boldsymbol{Q}, E) = \frac{\chi^{(0)}_{\alpha\beta}(E)}{1 - J_{\boldsymbol{Q}}\chi^{(0)}_{\alpha\beta}(E)}, \tag{6}$$

where $\chi^{(0)}(E)$ is the single-ion dynamical susceptibility calculated from the CEF eigenstates and $J_{\boldsymbol{Q}}$ is the Fourier transform of the real-space magnetic exchange interaction. The calculated scattering functions are shown in Fig. 11. Here, $J_{\boldsymbol{Q}}$ is treated as a parameter. The fact that the ordering occurs at $\boldsymbol{Q} = (1, 0, 0)$ means that $J_{\boldsymbol{Q}}$ becomes the largest at around $\boldsymbol{Q} = (1, 0, 0)$. At around $\boldsymbol{Q} = (0, 0, 1)$, on the other hand, $J_{\boldsymbol{Q}}$ should have a large negative value because (0, 0, 1) is far from the magnetic ordering propagation vector. If we assume $J_{\boldsymbol{Q}} = -5$ K, the decrease in intensity and the shift of the peak position to the higher energies can be reproduced well.

4.3 Successive phase transition

Let us study the successive phase transition through a mean-field calculation using the above CEF scheme. To describe the essence of the phenomenon concisely, we consider a simple two-sublattice model here, where only the interactions between the nearest-neighbor Dy atoms are taken into account; the next-nearest-neighbor interaction represented by the dashed lines in Fig. 9 is neglected. Although this might be a crude approximation, many aspects of the phenomenon can be explained as shown below. This may be because the moments of the next-nearest-neighbor ions are orthogonal with each other at zero field.

The Hamiltonian for the $\mathrm{Dy}^{(\mathrm{a})}$ sublattice is expressed as

$$\mathcal{H}_{\rm a} = \mathcal{H}_{\rm CEF} + \mathcal{H}_{\rm M} + \mathcal{H}_{\rm Q} + \mathcal{H}_{\rm Z} + \mathcal{H}_{\rm S}, \tag{7}$$

$$\mathcal{H}_{\rm M} = -J_\perp(J_x\langle J_x\rangle_{\rm b} + J_y\langle J_y\rangle_{\rm b}) - J_\parallel J_z\langle J_z\rangle_{\rm b}, \tag{8}$$

$$\mathcal{H}_{\rm Q} = -K_{\rm Q}(O_{zx}\langle O_{zx}\rangle_{\rm b} + O_{yz}\langle O_{yz}\rangle_{\rm b}), \tag{9}$$

$$\mathcal{H}_{\rm Z} = -\boldsymbol{\mu}\cdot\boldsymbol{H} = g\mu_{\rm B}\boldsymbol{J}\cdot\boldsymbol{H}, \tag{10}$$

$$\mathcal{H}_{\rm S} = -\sum_\gamma g_\gamma \varepsilon_\gamma O_\gamma\ ;\ \ (\gamma = 20, 22, yz, zx, xy). \tag{11}$$

$\mathcal{H}_{\rm M}$ is the magnetic exchange interaction with tetragonal anisotropy, $\mathcal{H}_{\rm Q}$ the quadrupolar exchange interaction for O_{yz} and O_{zx}, $\mathcal{H}_{\rm Z}$ the Zeeman effect in a uniform magnetic field, and $\mathcal{H}_{\rm S}$ the quadrupole-strain coupling that causes the local Jahn-Teller effect. The magnetic and stain susceptibilities are calculated with $\mathcal{H}_{\rm Z}$ and $\mathcal{H}_{\rm S}$, respectively. The elastic constant for the γ-type strain field is expressed as $C_\gamma = C^0_\gamma - Ng^2_\gamma\chi_\gamma$, where C^0_γ represents the nonmagnetic background elastic constant without f-electron effect, χ_γ the strain susceptibility defined by the relation of $\langle O_\gamma(\varepsilon_\gamma)\rangle - \langle O_\gamma(0)\rangle = \chi_\gamma g_\gamma \varepsilon_\gamma$, and $N = 2\times10^{22}$ cm^{-3} the number of Dy ions per unit volume. $\gamma = 20$ and 22 represent the $3z^2 - r^2$ and $x^2 - y^2$ types, respectively.

When both $\langle J_z\rangle$ and $\langle J_x\rangle$ become nonzero in phase III, $\langle O_{zx}\rangle$ also becomes nonzero because O_{zx} is expressed as $\sqrt{3}(J_zJ_x + J_xJ_z)/2$. Then, $\langle O_{zx}\rangle$ gives rise to a strain $\varepsilon_{zx} = Ng_{zx}\langle O_{zx}\rangle/C^0_{zx}$ through the $\mathcal{H}_{\rm S}$ term. Since $\langle J_z\rangle_{\rm a} = -\langle J_z\rangle_{\rm b}$, $\langle J_x\rangle_{\rm a} = -\langle J_x\rangle_{\rm b}$, and $\langle O_{zx}\rangle_{\rm a} = \langle O_{zx}\rangle_{\rm b}$ are satisfied in phase III, ε_{zx} for $\mathrm{Dy}^{(\mathrm{b})}$ is equal to that of $\mathrm{Dy}^{(\mathrm{a})}$. Therefore, in phase III, the $\mathcal{H}_{\rm S}$ term becomes numerically equivalent to the ferroquadrupolar interaction in the mean-field approximation.

If we set $J_\parallel = -0.67$ K, $J_\perp = -0.6$ K, $g_{zx} = 10$ K, and $K_{\rm Q} = 0$ K, there appear two phase transitions at $T_{\rm N1} = 20$ K and $T_{\rm N2} = 12.5$ K, which coincide with the actual values of DyB_4. The quadrupole-strain coupling constant of the order of 10 K should be fixed in order to explain the paramagnetic softening of the elastic constants reported in ref. 14. If we assume $g_{yz} = g_{zx}$ and evaluate $C_{44} = C^0_{44} - N(g^2_{yz}\chi_{yz} + g^2_{zx}\chi_{zx})/2$ using the calculated strain susceptibilities χ_{yz} and χ_{zx} shown below, the paramagnetic softening of C_{44} of the order of 0.3×10^{11} erg/cm^3 can be reasonably explained. We have neglected the $\mathcal{H}_{\rm Q}$ term for simplicity because it is numerically absorbed in the $\mathcal{H}_{\rm S}$ term in phase III, and also because the effect of $K_{\rm Q}$ can be compensated for to some extent by tuning $J_\perp$.

The temperature dependences of the calculated physical properties are shown in Fig. 12. With decreasing the temperature, $\langle J_z\rangle$ first appears at $T_{\rm N1} = 20$ K, followed by the appearance of $\langle J_x\rangle$ and $\langle O_{zx}\rangle$ at $T_{\rm N2} = 12.5$ K. The magnetic susceptibility for $H \perp c$ keeps increasing with decreasing the temperature through $T_{\rm N1}$. The calculated results well reproduce the actual behavior in DyB_4 except for the SRO of $\langle J_x\rangle$ in phase II. The existence of $\langle O_{zx}\rangle$ in phase III is confirmed by RXD.[17] The calculated strain $\varepsilon_{zx} = Ng_{zx}\langle O_{zx}\rangle/C^0_{zx}$ is also consistent

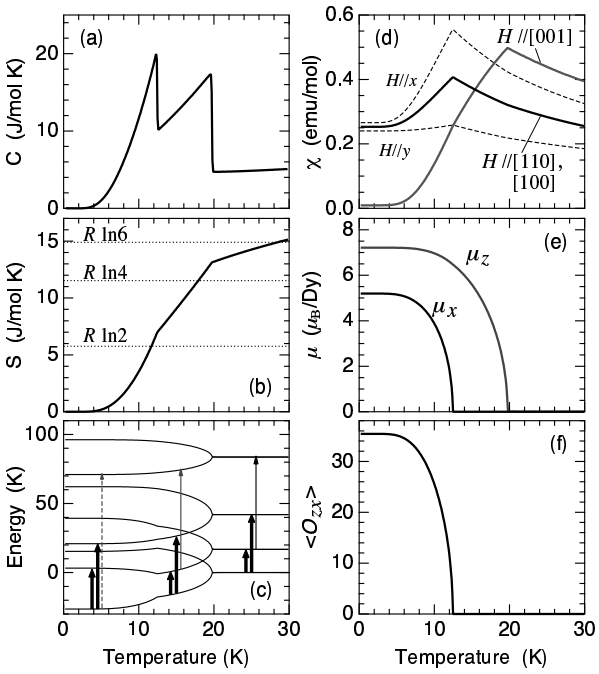

Fig. 12. Calculated temperature dependences of (a) specific heat, (b) magnetic entropy, (c) energy level, (d) magnetic susceptibility, (e) components of ordered magnetic moments, and (f) ordered quadrupole moment $\langle O_{zx}\rangle$. The arrows in (c) represent the three strongest excitations in the calculated neutron scattering intensity at $\boldsymbol{Q} = (1, 0, 0)$. The thickness roughly represents the transition strength.

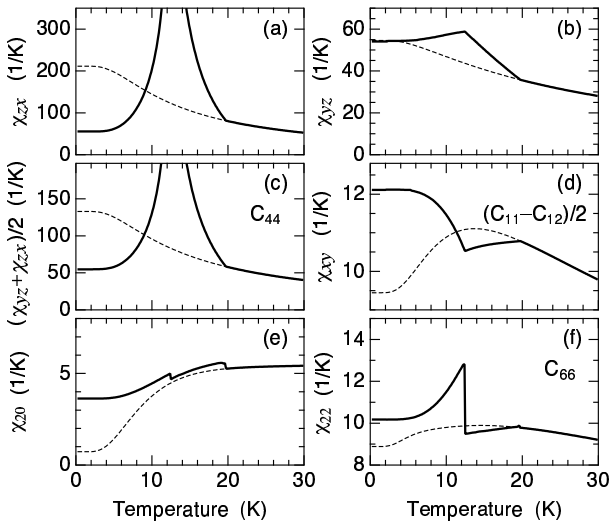

Fig. 13. Calculated temperature dependences of the strain susceptibilities. The dashed lines are for the paramagnetic state. The corresponding elastic-constant mode is shown in (c), (d), and (f).

with the monoclinic distortion reported in refs. 15, 17, and 24; ε_{zx} is estimated to be 4.2×10^{-3} at $T = 0$ K if we assume $C^0_{zx} = 2.3 \times 10^{11}$ erg/cm^3 from the C_{44} data in ref. 14. This ε_{zx} corresponds to the monoclinic angle with $90° - \beta = 0.26°$ at $T = 0$ K and 0.18° at $T = 10$ K, which is consistent with the experimental result.

It should be remarked that the experimental magnetic entropy is well reproduced in this calculation; $R \ln 2$ is released at $T_{\rm N2}$, and $R \ln 4$ at $T_{\rm N1}$.[14] In previous reports, it has been discussed that a kind of degeneracy, possibly of quadrupolar one, somehow remains even in phase II and is lifted in phase III.[14,15,17] However, the mean-field calculation here shows that this interpretation is misdirected. $R \ln 2$ at $T_{\rm N2}$ is an accidental coincidence. As shown in Fig. 12(c), all the doublets are split by the magnetic ordering at $T_{\rm N1}$ and no degeneracy remains. The additional ordering at $T_{\rm N2}$ occurs because the total free energy can be further reduced by adding the x-component.

The temperature dependence of E_1 shown in Fig. 7 can also be understood qualitatively from the diagram of Fig. 12(c). In the paramagnetic phase I, the experimentally observed excitation at E_1 can purely be ascribed to the CEF excitation from the ground doublet to the first excited doublet. On the other hand, in the magnetically ordered phases II and III, the nature of the excitation at E_1 changes to the transition between the split singlets. The excitation energy does not change much between phases I and II, whereas it increases in phase III, well explaining the experimental result in Fig. 7. With respect to the second (E_2) and third (E_3) excitations, the agreement with the experimental result shown in Fig. 6 is not satisfactory, especially concerning the change in intensity. The remaining discrepancies may be due to the simplicity of the present model neglecting the actual lattice structure. In addition, in phases II and III, the spin-wave character is mixed with the CEF excitation, which should be taken into account for a more exact treatment.[25]

Figure 13 shows the temperature dependences of the calculated strain susceptibilities. It is noted that an increase in χ_γ corresponds to a softening in C_γ. Also note that C_γ indicated in Fig. 13 is defined with respect to the tetragonal crystal axes, whereas χ_γ with respect to the local axes. Therefore, C_{44} corresponds to $(\chi_{yz} + \chi_{zx})/2$, $(C_{11} - C_{12})/2$ to χ_{xy}, and so on. We see that the paramagnetic strain susceptibility χ_{zx} is much larger than the others. This is purely a CEF effect and leads to the relatively large paramagnetic softening in the C_{44} mode, as reported in ref. 14.

The most important result here is that the huge elastic softening in the C_{44} mode below $T_{\rm N1}$ is well reproduced by the mean-field calculation, as shown in Fig. 13(c). This huge softening in the calculation is caused by the abrupt increase in χ_{zx} below $T_{\rm N1}$. The reason for the abrupt increase in χ_{zx} is that the $\langle O_{zx}\rangle$ moment is induced much more effectively in the antiferromagnetic ordered state with $\langle J_z\rangle_{\rm a} = -\langle J_z\rangle_{\rm b}$ than in the paramagnetic state with $\langle J_z\rangle = 0$. Since the magnetic moments can be relatively easily canted from the z axis to the x axis in the present CEF anisotropy, ε_{zx}-type strain induces $\langle J_x\rangle_{\rm a} = -\langle J_x\rangle_{\rm b}$ in phase II, and therefore much larger $\langle O_{zx}\rangle$ moments are induced than in phase I. The antiferromagnetic state with $\langle J_x\rangle_{\rm a} = -\langle J_x\rangle_{\rm b}$ induced by the external strain is identical to the ordered state below $T_{\rm N2}$, which leads to the divergent behavior of χ_{zx} towards $T_{\rm N2}$.

Finally, we note that the main driving force realizing phase III is the characteristic CEF anisotropy explained in §4.1 and the magnetic exchange interaction. The quadrupole-strain coupling and resultant ferroquadrupolar interaction have little effect on the phase transitions. Even if we change $K_{\rm Q}$ and g_{zx} and tune $J_\perp$ to keep $T_{\rm N2}$ at 12.5 K, main features of Figs. 12 and 13 do not change.

5. Discussion

In previous reports, it was discussed that J_x and O_{zx} are disordered and that the doublet degeneracy somehow remains even in phase II in which J_z is ordered.[14,15,17] It was also discussed that this might be associated with a geometrical frustration. However, we consider that this interpretation is not the case. The mean-field calculation simply demonstrates that the magnetic moment along the z-axis tilts to the x-axis at $T_{\rm N2}$ simultaneously with the appearance of $\langle O_{zx}\rangle$ and ε_{zx}. In terms of quadrupolar moments, the pancake-like charge distribution of the O_{20} moment tilts to the x-axis to give rise to $\langle O_{zx}\rangle$ and a monoclinic distortion. The double transition in DyB_4 can simply be described by the mean-field calculation performed in §4, even without considering an interionic quadrupolar interaction explicitly. In spite of the simplicity of the model, most of the macroscopic properties were explained.

On the other hand, the short-range order of J_x observed by RXD and ND is one of the characteristic phenomena in DyB_4, which is beyond the description by the mean-field calculation. Although this SRO seems static by RXD and ND, this is actually a dynamic fluctuation when viewed from magnetic susceptibility and elastic constant measurements. The increase in $\chi(T)$ for $H \perp c$ and the softening of $C_{44}(T)$ with decreasing T observed experimentally would not be expected if the ordering were completely static. The softening of the C_{44} shows that the fluctuation of the SRO can follow the oscillation of ultrasonic strain field at a frequency of several tens of MHz, which means that the time scale of the fluctuation is shorter than $\sim 10^{-8}$ s. In view of the significant ultrasonic attenuation in phase II,[14] it is expected to be much longer than the lower limit of $\sim 10^{-11}$ s as estimated by ND. In addition, what is anomalous is that the correlation length of the SRO is quite large; the length is estimated to be $\sim 1.4 \times 10^3$ Å by RXD, although we have to keep in mind that the correlation length of the bulk can be different from that in the surface region observed by RXD.[15] However, we also note that all the Bragg peaks in ND experiments were resolution-limited, indicating that the correlation length of the bulk is also quite large. Thus, in phase II, the ordered structure finally accomplished in phase III develops as a large fluctuation with slow dynamics. This may be associated with the enhanced strain susceptibility of χ_{zx} in phase II.

It would be interesting if the SRO of O_{zx} without the monoclinic strain were detected in phase II by RXD. This should be possible in the σ-σ' channel at $\Psi = 45°$, as has been observed for the static LRO of O_{zx} in phase III.[17] If $\langle J_x\rangle$ exists already in phase II, $\langle O_{zx}\rangle$ is expected to accompany and should be detected experimentally.

We need to recognize, though contrary to the initial motivation, that the effect of SSL is hardly observed at zero field. However, it is definitely necessary to take into account the actual lattice structure to interpret the complex multistep magnetization process in the RB_4 systems. For DyB_4, the magnetic phase diagram reported in refs. 21 and 26 can never be reproduced by the two sublattice model studied here. The field-induced magnetic phases reported on TbB_4 and TmB_4 also require consideration of the actual lattice structure.[7–11,19]

6. Conclusions

We have studied the successive phase transition in DyB_4 by RXD and neutron scattering. Both methods show that the *ab*-plane component of the magnetic moment is short-range-ordered in phase II. This is considered to be a dynamical short-range order since the bulk properties are paramagnetic. The time scale of the fluctuation in phase II has been discussed from the results of ND and ultrasonic experiments. We have also succeeded in observing crystal field excitation by inelastic neutron scattering.

To interpret the nature of the phase transition, we studied a simple two-sublattice model by mean-field calculation. By introducing fourth-order terms of the crystal field Hamiltonian as large as second order terms, we have shown that the essential aspects of the phenomenon at zero field can be explained mainly by an antiferromagnetic exchange interaction. Since most of the macroscopic properties can be explained by this simple calculation, the characteristic lattice structure with geometrical frustration and the interionic quadrupolar exchange interactions seem to have little effect at least in zero field.

Acknowledgment

The authors thank R. Watanuki, H. Onodera, M. Sera, and A. Tanaka for many fruitful discussions. We also thank M. Onodera for assistance in crystal growth, K. Nemoto and Y. Wakabayashi for support to experiments performed in JRR-3 and Photon Factory, respectively. This work was supported by a Grant-in-Aid for Scientific Research from the Japan Society for the Promotion of Science (JSPS) and also by the 21st century COE program of Tohoku University.

1) M. Mekata: J. Magn. Magn. Mater. **90&91** (1990) 247.
2) M. Mekata: J. Phys. Soc. Jpn. **42** (1977) 76.
3) H. Kadowaki, K. Ubukoshi, and K. Hirakawa: J. Phys. Soc. Jpn. **56** (1987) 751.
4) B. S. Shastry and B. Sutherland: Physica B **108** (1981) 1069.
5) H. Kageyama, K. Yoshimura, R. Stern, N. V. Mushnikov, K. Onizuka, M. Kato, K. Kosuge, C. P. Slichter, T. Goto, and Y. Ueda: Phys. Rev. Lett. **82** (1999) 3168.
6) Z. Fisk, M. B. Maple, D. C. Johnston, and L. D. Woolf: Solid State Commun. **39** (1981) 1189.
7) S. Yoshii, T. Yamamoto, M. Hagiwara, S. Michimura, A. Shigekawa, F. Iga, T. Takabatake, and K. Kindo: Phys. Rev. Lett. **101** (2008) 087202.
8) T. Inami, K. Ohwada, Y. H. Matsuda, Z. W. Ouyang, H. Nojiri, T. Matsumura, D. Okuyama, and Y. Murakami: J. Phys. Soc. Jpn. **78** (2009) 033707.
9) S. Yoshii, K. Ohoyama, K. Kurosawa, H. Nojiri, M. Matsuda, P. Frings, F. Duc, B. Vignolle, G. L. J. A. Rikken, L.-P. Regnault, S. Michimura, and F. Iga: Phys. Rev. Lett. **103** (2009) 077203.

10) K. Siemensmeyer, E. Wulf, H.-J. Mikeska, K. Flachbart, S. Gabáni, S. Mat'aš, P. Priputen, A. Efdokimova, and N. Shitsevalova: Phys. Rev. Lett. **101** (2008) 177201.
11) S. Michimura, A. Shigekawa, F. Iga, T. Takabatake, and K. Ohoyama: J. Phys. Soc. Jpn. **78** (2009) 024707.
12) R. Watanuki, T. Kobayashi, R. Noguchi, and K. Suzuki: J. Phys.: Conf. Ser. **150** (2009) 042229.
13) T. Matsumura, D. Okuyama, and Y. Murakami: J. Phys. Soc. Jpn. **76** (2007) 015001.
14) R. Watanuki, G. Sato, K. Suzuki, M. Ishihara, T. Yanagisawa, Y. Nemoto, and T. Goto: J. Phys. Soc. Jpn. **74** (2005) 2169.
15) D. Okuyama, T. Matsumura, H. Nakao, and Y. Murakami: J. Phys. Soc. Jpn. **74** (2005) 2434.
16) D. Okuyama, T. Matsumura, T. Mouri, N. Ishikawa, K. Ohoyama, H. Hiraka, H. Nakao, K. Iwasa, and Y. Murakami: J. Phys. Soc. Jpn. **77** (2008) 044709.
17) S. Ji, C. Song, J. Koo, J. Park, Y. J. Park, K.-B. Lee, S. Lee, J.-G. Park, J. Y. Kim, B. K. Cho, K.-P. Hong, C.-H. Lee, and F. Iga: Phys. Rev. Lett. **99** (2007) 076401.
18) W. Schäfer, G. Will, and K. H. J. Buschow: J. Chem. Phys. **64** (1976) 1994.
19) A. Tanaka: presented at the JPS 2009 Autumn Meeting, 25pPSA-58.
20) According to R. Watanuki, neutron powder diffraction analysis shows that Model II (two-in two-out) is the case with respect to the magnetic structure. This is not determined in ref. 17.
21) R. Watanuki: Ph.D. thesis, Yokohama National University (2004).
22) We showed the result for (1, 0, 0) here because the energy resolution was the highest. Although the sensitivity to the fluctuation of the *ab*-plane component becomes better with larger index l, the width of the Bragg peak at $E = 0$ also increases because of the resolution degradation, making the observation of the critical scattering difficult.
23) M. T. Hutchings, in *Solid State Physics*, ed. F. Seitz and D. Turnbull (Academic Press Inc., New York, 1964) Vol. 16, p. 227.
24) D. Okuyama, T. Matsumura, H. Nakao and Y. Murakami: J. Phys. Soc. Jpn. **75** Suppl. (2006) 198.
25) T. M. Holden, E. C. Svensson, W. J. L. Buyers, and O. Vogt: Phys. Rev. B **10** (1974) 3864.
26) R. Watanuki, H. Mitamura, T. Sakakibara, G. Sato, and K. Suzuki: Physica B **378-380** (2006) 594.